Electrochimica Acta 446 (2023) 142060

Contents lists available at ScienceDirect

Electrochimica Acta

journal homepage: www.journals.elsevier.com/electrochimica-acta

Structural, morphological and electrochemical characterization of the degradation processes during the oxygen reduction reaction of iron(II) phthalocyanine supported on carbon nanotubes

Simon-Johannes Kinkelin, Matthias Steimecke, Emil Dieterich, Michael Bron *

Institut für Chemie; Technische Chemie I, Martin-Luther-Universität Halle-Wittenberg, Von-Danckelmann-Platz 4, 06120, Halle Saale, Germany

ARTICLE INFO

Keywords:
Oxygen reduction reaction
Non-noble metal catalyst
Degradation mechanism
in situ-Raman microscopy
X-ray photoelectron spectroscopy

ABSTRACT

A non-noble metal catalyst (Fe-N_x@MWCNTs), which was prepared by wet impregnation of surface-functionalized multi-walled carbon nanotubes (MWCNTs) with iron(II) phthalocyanine (FePc) and heat treatment, as well as the functionalized MWCNTs without FePc were examined towards their performance for the oxygen reduction reaction (ORR) in neutral media and their structural properties during electrochemically forced degradation. Electroanalytical methods as well as *in situ*-Raman microscopy and *ex situ*-X-ray photoelectron spectroscopy (XPS) were applied at different levels of a two-stage accelerated stress test (AST). In particular, the comparability between the electrochemical, the *in situ*-Raman and the *ex situ*-XPS setup was confirmed. It was found that the iron central atom was leached out of the Fe-N_x-complex during the first stage of the AST causing a decline of ORR activity, still higher than that of the MWCNT support, which remained unaffected. During the second stage, the samples were subjected to stronger electrochemical stress by cycling to highly positive potentials, causing the formation of surface groups and an increase of double layer capacitance. The high potentials also destroy remaining catalytic N—C moieties and the ORR activity of the catalyst approaches that of the bare support. With ongoing AST cycling, the overall current of the samples is heavily reduced which is attributed to loss of electric conductivity of the sample backbone by further oxidation.

1. Introduction

Fuel cells are considered to play a key role for electrochemical energy conversion of sustainably produced hydrogen in stationary as well as automotive applications. However, the cost of the system components of fuel cells, and in particular the noble metal-based catalysts necessary for improving the sluggish oxygen reduction reaction (ORR) at the cathode, impede a broad market implementation of this technology. On this account, huge effort is devoted to designing non-noble metal (NNM) catalysts with good performance for the ORR as well as high stability in acidic and alkaline media. Among a wealth of NNM catalysts [1,2], metal-nitrogen catalysts supported on a high surface area carbon material (M-N@C, where M denotes the non-noble metal, which is most commonly Fe or Co) were found to exhibit remarkable performance for the ORR [1–7] and are therefore, besides fuel cells, also of great interest as cathode material in metal air batteries [8]. These catalysts are commonly prepared by heat treating a mixture of M- as well as N-containing precursors with the carbonaceous supporting material. The choice of the carbon support as well as of the M- and N-containing precursors, the amount of metal species and the temperature during heat treatment strongly influence the catalyst structure as well as the resulting electrochemical performance [4,6,9,10]. However, it is still not entirely clear which kind of M-N_x moiety exactly acts as active site or whether the metal species is just crucial for the formation of active sites during the pyrolysis process, while activity of individual sites might also depend on the electrolyte solution [11–17].

Indeed, M-N@C catalysts show high electrochemical performance for the ORR in both acidic and alkaline media. However, they suffer from low stability especially in acidic environment. Six different mechanisms causing degradation are discussed: (1) destruction of the carbonaceous support by carbon corrosion, (2) leaching of the metal ion, (3) attack by free radicals (e.g. from H_2O_2), (4) poisoning of active pyridinic CN_x sites by protonation, (5) exchange of protons in the ionomer with leached metal ions from the M-N@C catalyst and (6) flooding of the catalyst pores with water [10,18]. Therefore, huge effort is undertaken to investigate the stability of M-N@C materials as well as the

* Corresponding author.
E-mail address: michael.bron@chemie.uni-halle.de (M. Bron).

https://doi.org/10.1016/j.electacta.2023.142060
Received 1 September 2022; Received in revised form 14 February 2023; Accepted 14 February 2023
Available online 15 February 2023

corresponding degradation pathways [10,19–23].

In this work, an accelerated stress test (AST) protocol was applied to an iron(II)-phthalocyanine (FePc) based catalyst material supported on surface functionalized multi-walled carbon nanotubes (MWCNTs). Besides electrochemical techniques also structural methods were used in order to perform an in-depth investigation of the degradation processes. FePc is a prominent candidate with excellent electrocatalytic performance towards the ORR, as already shown elsewhere [8,21,24–26]. In this particular study, the stability experiments were conducted employing a three-electrode setup and porous thin-film electrodes in 1 M KCl / 0.1 M phosphate-buffer (PBS) electrolyte solution at pH = 6.5 to exclude influences of the membrane-electrode-interface. The neutral electrolyte with PBS for pH-control was chosen to avoid pH-related degradation mechanisms, intended leaching of the Fe central atom by formation of $FePO_4$ as well as facilitating *in situ*-Raman experiments, which are much more demanding in strongly acid or alkaline solutions due to materials challenges. Thus, the above-mentioned degradation processes (4), (5) and (6) are not addressed in this work and the focus is on processes (1), (2) and (3). A two-stage AST protocol was applied with the aim of (i) stressing only the active sites of the Fe-N_x@MWCNT catalyst and (ii) affecting the structure of both the phthalocyanine complex as well as the carbonaceous support. During the AST protocol, the electrochemical and structural properties of the investigated materials were monitored. For structural characterization *in situ*-Raman microscopy as well as *ex situ*-X-ray photoelectron spectroscopy were performed to investigate the defect structure of the carbon lattice respectively changes of the surface atomic composition.

2. Experimental

2.1. MWCNT functionalization and Fe-N_x@MWCNT synthesis

Functionalized multiwalled carbon nanotubes (MWCNTs) were used as support for the preparation of Fe-N_x@MWCNT catalysts. Pretreatment and functionalization followed a reported procedure [27]: high purity MWCNTs (Baytubes® C 150 P, >95%) were heat treated in a tube oven (Gero SR-A 70–500/12) in Ar atmosphere. A quartz glass boat containing the MWCNTs was inserted into a quartz glass tube, which was purged with argon gas for 15 min to drive out all other gases. The material was heated from room temperature up to 50 °C within 15 min and this temperature was kept constant for 15 min to equilibrate the system. Afterwards, the oven was heated up to 800 °C with 10 K min^{-1} and the final temperature was kept for 15 min. The resulting material was labeled MWCNT_800. To obtain functionalized MWCNTs, 500 mg of MWCNT_800 was mixed with 32 ml nitric acid (Roth, 65%) and 100 ml deionized water (0.055 µS cm^{-1}) in a glass flask. To achieve a homogeneous suspension, the flask was placed in an ultrasonic bath for 30 min. Afterwards, it was transferred to a microwave oven (START, MLS GmbH) and heated under reflux for 1 h and 5 min at 800 W pulsed irradiation power, keeping the temperature in the reaction mixture constant at ~100 °C. The suspension was stirred continuously with a magnetic stirrer. After cooling down to below 40 °C, the MWCNTs were washed with deionized water several times until pH = 7 was reached, using a centrifuge (Eppendorf centrifuge 4807) for separation. The sample was dried in ambient atmosphere at 100 °C for several hours. In the following, this material is named as 'support' or labeled as 'Sup.'.

This supporting material was modified with iron(II) phthalocyanine (FePc, TCI Chemicals, >95%) by wet impregnation applying an adapted synthesis route of Schulenburg et al. [28]. To obtain a final iron content of ~2.0 wt.-%, 101.9 mg FePc were dissolved in 400 ml acetone (Roth) in a round-bottom flask, stirred with a magnetic stirrer at 350 rpm for 30 min and placed in an ultrasonic bath for another 30 min. After adding 399.6 mg of the MWCNT support, the mixture was again stirred for one hour at 350 rpm and placed in an ultrasonic bath for another hour. The well mixed slurry was transferred to a beaker and the acetone was evaporated under continuous stirring at 35 °C overnight. Afterwards, the material was transferred to a quartz glass boat and heat treated in a tube oven (Gero SR-A 70–500/12) under Ar atmosphere. The tube was purged with Ar for 15 min before heating up to 50 °C within 15 min. To equilibrate the system, this temperature was kept constant for another 15 min. Finally, the temperature was increased to 600 °C with 10 K min^{-1} and kept constant for 2 h. The sample is referred to as 'catalyst' or is labeled as 'Cat.' throughout the text.

2.2. Characterization

2.2.1. Surface area determination

Specific surface area determination based on nitrogen adsorption was carried out with a Sorptomatic 1990 (Thermo Finnigan). Prior to analysis, the samples were heated under vacuum (10^{-5} mbar) at 120 °C for 24 h. Adsorption and desorption isotherms were recorded at 77 K using nitrogen as adsorbate at relative pressures p/p_0 of 0.05 to 0.3. The evaluation of adsorption data was done applying the Brunnauer-Emmett-Teller (BET) theory. The determined specific surface areas are denoted as SSA_{BET}.

2.2.2. Thermogravimetric analysis (TGA)

Thermogravimetric analysis was performed with a STA449 F1 Jupiter® thermobalance (Netzsch) in an aluminum oxide crucible. Prior to the measurements, the heating chamber was evaporated and subsequently flushed with Ar for three times to remove oxygen impurities. The TGA was performed either in an Ar flux (50 ml min^{-1}) or a mixture of Ar (45 ml min^{-1}) and oxygen (5 ml min^{-1}). The sample was initially kept at 35 °C for 15 min and in the following heated with 10 K min^{-1} up to 1200 °C.

2.2.3. Electrochemical characterization

Electrochemical measurements were performed employing a glassy carbon (GC) electrode (4 mm diameter, Sigradur® G, HTW Hochtemperatur-Werkstoffe, embedded in a PTFE cylinder), which was modified with a porous thin-film by drop-casting inks of the synthesized samples (Sup. respectively Cat.) onto the GC tip. The inks with a loading of 6.28 µg $µl^{-1}$ were prepared by mixing approximately 5 mg of the particular sample with approximately 800 µl of isopropanol containing Nafion® 117 solution (5 wt.% in lower aliphatic alcohols, Sigma-Aldrich) with a ratio $V_{isopropanol}/V_{Nafion\text{-}sol.}$ = 48:2. The mixtures were stirred with a magnetic stirrer for 5 min at 500 rpm and subsequently placed in an ultrasonic bath thermostatically kept at 20 °C for 1 h. During this time, the samples were shaken cautiously several times to avoid aggregation of sample material at the bottom of the tube. Afterwards, two times 3 µl of the particular ink were drop-casted onto the GC tip to obtain a sample loading of 300 µg cm^{-2}. Beforehand, the GC tip was polished with alumina paste (1.0 and 0.3 µm) as well as water on polishing cloth for at least 3 min each until a mirror-like finish was obtained.

The electrochemical measurements were carried out with an Autolab PGSTAT128N potentiostat (Metrohm) in a glass cell using a three-electrode setup. The coated GC tip served as working electrode (WE), an Ag|AgCl|KCl_{sat} electrode as reference electrode (RE) and a Pt wire as counter electrode (CE). The GC tip was mounted onto a rotating device (Radiometer INF-EL-EDI 101) controlled by a speed control unit (Analytical CTV 191) in order to perform RDE measurements. All measurements were performed in 1 M KCl solution buffered with 0.1 M PBS (50 mM KH_2PO_4 and 50 mM K_2HPO_4) at pH = 6.5. The potential of the RE was determined to be 0.57 V vs. RHE in the applied electrolyte solution and in the following, all potentials are given against RHE.

Electrochemical characterization and the accelerated stress test (AST) protocol were carried out as follows. First, the electrode was equilibrated by performing 100 cyclic voltammograms (CVs) with 500 mV s^{-1} scan rate v between −0.03 and 1.37 V vs. RHE in N_2 purged electrolyte. To identify non-faradaic currents, linear sweep voltammetry with a rotating disk electrode (LSV-RDE) at different rotation velocities

(400, 900, 1600 and 2500 rpm) between −0.13 and 0.97 V vs. RHE with $\nu = 5$ mV s^{-1} as well as CV between −0.03 and 1.37 V vs. RHE with $\nu =$ 50 mV s^{-1} and 500 mV s^{-1}, respectively, were carried out in the very same electrolyte. Moreover, electrochemical impedance spectroscopy (EIS) was conducted between 50 kHz and 0.1 Hz at 0.87 V vs. RHE with 5 mV amplitude (Root Mean Square) to investigate the uncompensated resistance R_U and the double layer capacitance of the electrode interface C_{DL}. LSV-RDE, CV and EIS measurements were repeated with the same parameters in O_2 purged electrolyte as initial electrochemical characterization at the begin of testing (BoT). Afterwards, 500 CVs between 0.57 and 1.57 V vs. RHE (denoted as 'AST1.6′ in the following) and subsequently 2000 CVs between 0.87 and 1.87 V vs. RHE (denoted as 'AST1.9′ in the following) were performed with $\nu = 500$ mV s^{-1} in O_2 purged electrolyte to impose electrochemical stress onto the samples at two different severities. During AST1.6 every 125 cycles and during AST1.9 every 250 cycles LSV-RDE with 1600 rpm, CV and EIS as described above were carried out to characterize the electrochemical behavior. Furthermore, after 500 cycles of AST1.6 as well as 750 and 2000 cycles of AST1.9 LSV-RDE with 400, 900, 1600 and 2500 rpm was performed. This procedure was applied three times at separately prepared porous thin-film electrodes of both samples in order to ensure reproducibility. The LSV-RDE curves obtained in N_2 purged electrolyte were subtracted from those obtained in O_2 purged electrolyte for double layer correction and the obtained curves were corrected with the uncompensated resistance determined by EIS at 50 kHz.

2.2.4. *In situ-Raman microscopy*

For Raman spectroscopy an InVia Raman spectrometer (Renishaw) with a microscope (Leica) equipped with a water immersion objective (63x, Leica), a Cobolt CW DPSS laser (532 nm excitation wavelength), a 1800 l mm^{-1} grating and a Peltier cooled charge coupled device (CCD) camera detecting the Raman scattering were used. Prior to use, the Raman spectrometer was calibrated to a silicon reference peak and the signal was adjusted to 520.4 cm^{-1}. The measurements were carried out in an *in situ*-cell combining an electrochemical three electrode setup with the InVia Raman spectrometer and allowing for electrochemical measurements during or in between the Raman investigation. For *in situ*-characterization, a Raman mapping was performed at 49 measurement points with a distance of 1.5 μm in x- and y-direction between each measurement point. The spectra were recorded at 900 - 1800 cm^{-1} with 5 % laser intensity (~1.5 mW laser power) and 15 s integration time.

In this case, the electrochemical characterization was conducted solely in O_2 purged electrolyte and neither LSV-RDE nor EIS was performed. *In situ*-Raman spectra were recorded as described above after initial characterization at the BoT, 500 AST1.6 cycles as well as 750 and 2000 AST1.9 cycles (i.e. 1250 and 2500 cycles in total) at the very same sample position. The obtained spectra were post-processed by subtracting a linear baseline, whose boundary values were calculated between 900 and 925 cm^{-1} respectively 1773 and 1797 cm^{-1}, to compensate for background noise. The baseline corrected spectra were then normalized to their particular maximum and average values as well as standard deviations were calculated for all Raman spectra recorded at the same AST level for the two samples, respectively.

2.2.5. *Ex situ-X-ray photoelectron spectroscopy (XPS)*

Surface characterization of the materials was carried out by X-ray photoelectron spectroscopy (XPS) using a DAR 400 instrument (Omicron) with an Al K_α line (1486 eV, 250 W) as X-ray source and an EA 125X Hemispherical Energy Analyzer (Omicron). Survey scans were performed with 200 eV pass energy, detail scans of the O 1s, N 1s and Fe 2p regions with 30 eV. The spectra were fitted and analyzed using the Casa XPS software. A Shirley background was subtracted from all spectra.

For *ex situ*-X-ray photoelectron spectroscopy 24 μl of the particular ink were drop-casted onto a square GC Chip (1 cm^2 geometric area, Sigradur® G, HTW Hochtemperatur-Werkstoffe) to obtain 150 μg cm^{-2} sample loading. The inks were prepared as described above, but Nafion® was not added to the solution, due to its intense fluorine response in XPS. The electrochemical measurements were carried out exclusively in O_2-purged electrolyte, the procedure was implemented as described in chapter 2.2.3 without LSV-RDE and, in contrast to all the other experiments, a Pt mesh was used instead of a Pt wire as counter electrode to ensure sufficiently fast counter reaction. XPS was performed after the initial characterization at the BoT as well as after 500 respectively at least 1250 AST1.9 cycles at both the support and the catalyst. At the catalyst, *ex situ*-XPS was additionally performed after 500 AST1.6 cycles. To remove residual ions, the electrode film was placed in deionized water for a few minutes whenever it was removed from the electrolyte solution. Despite special care was taken to prevent destruction of the sample film, sometimes a detachment of some material from the substrate was optically noticed while removing it from the deionized water, after performing the whole AST protocol.

Table 1
Specific surface area determined by BET analysis (SSA_{BET}) and mass loss during TGA up to 1000 °C in oxygen-free (Δm_{Ar}) as well as oxygen-containing atmosphere (Δm_{O2}; 10 vol.-% oxygen in argon).

Sample	SSA_{BET} / m^2 g^{-1}	Δm_{Ar} /%	Δm_{O2} /%
MWCNT_800	169	1.2	97.0
Sup.	192	4.6	97.8
Cat.	157	5.0	94.9

Table 2
Surface atomic compositions extracted from XPS survey scans of the powder materials for the characteristic binding energies of C 1s (284 eV), O 1s (531 - 532 eV), N 1s (398 - 399 eV), Fe 2p (709 – 710 eV).

Sample	C 1s / at%	O 1s / at%	N 1s / at%	Fe 2p / at%
MWCNT	98.3	1.6	–	0.1
Sup.	96.9	3.1	–	–
FePc	77.7	3.6	17.8	0.9
Cat.	95.2	2.4	2.2	0.2

3. Results and discussion

3.1. *Structural characterization of the powder materials*

An oxygen reduction catalyst was prepared by wet impregnation of an oxidized carbon nanotube support with iron(II) phthalocyanine followed by high temperature treatment at 600 °C. The obtained catalyst as well as the precursor materials were investigated with nitrogen adsorption towards their specific surface area (SSA_{BET}), with TGA and XPS concerning their chemical composition and with Raman spectroscopy for structural analysis.

Table 1 summarizes results from BET and TGA measurements of all samples. The SSA_{BET} of the starting material MWCNT_800 was obviously increased by the microwave acid treatment ("Sup."). Moreover, TGA in Ar atmosphere shows a higher weight loss of the support compared to the starting material, which is attributed to decomposition of oxygen-containing groups formed at the surface (Table 1 and Fig. SI-1 (supporting information)), which increase the surface area and porosity of the sample similarly as reported in literature [27,29]. Additionally, the MWCNT material and the support exhibit relatively high residual mass after TG in oxygen containing atmosphere, indicating that both materials contain metal impurities. Therefore, XPS was performed at the as-received MWCNTs to obtain information about their elemental composition, and besides carbon and oxygen only iron, probably originating from the MWCNT growth process, contributes to the survey spectrum appreciably (Table 2 and Fig. SI-2). Impregnation of the support with FePc and subsequent heat treatment at 600 °C results in smaller SSA_{BET} for the synthesized ORR catalyst in comparison to the

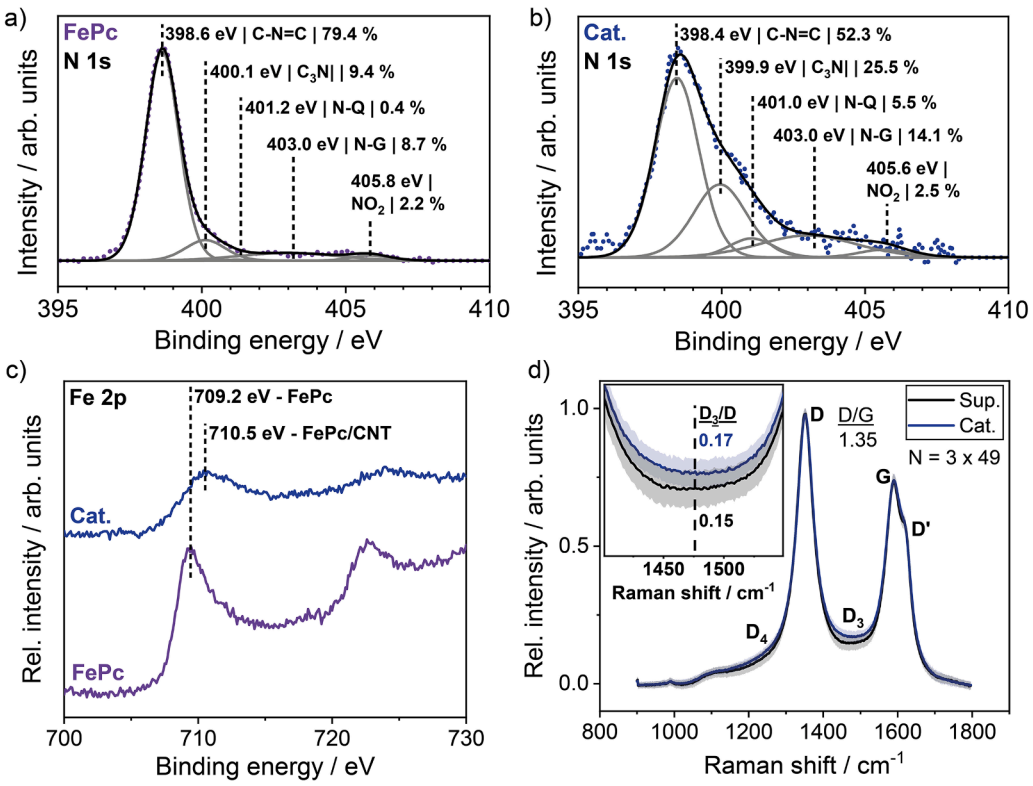

Fig. 1. XPS detail scans of the N 1s region of a) FePc and b) the catalyst as well as c) the corresponding detail scans of the Fe 2p region and d) Raman spectra of support and catalyst. In a) and b) the measured data is displayed with colored dots, the fitted spectra with black lines and the spectrum deconvolution with gray lines. Binding energies of the contributions to the N 1s region were attributed according to [30, 31]. The spectra in d) are displayed as mean values with standard deviation, represented by the brightly colored areas, calculated from 49 Raman mapping points at three separately prepared thin-film electrodes, respectively.

support, which can be explained by pore filling with complex or its decomposition products as well as associated increase of gravimetric density. The effective amount of iron in the catalyst was determined to be 2.9 wt.% by TGA in oxygen containing atmosphere (Table 1 (difference between weight loss of Sup. and Cat.) and Fig. SI-1). Quantitative XPS analysis, as summarized in Table 2, reveals that the oxygen containing groups introduced into the support by acid treatment are partially removed after catalyst formation (impregnation and heat treatment at 600 °C) and iron-nitrogen compounds were successfully attached to the carbonaceous supporting material. XPS detail scans were

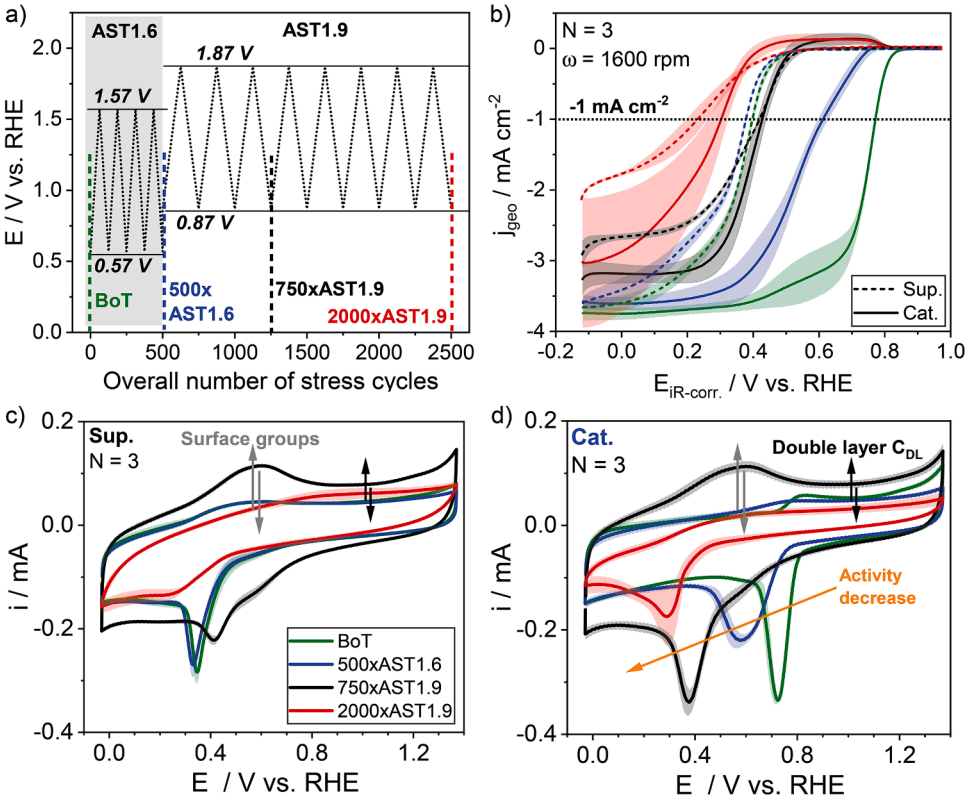

Fig. 2. a) Schematic of the two-stage AST protocol with the corresponding stages, b) double layer corrected linear sweep voltammogramms (5 mV s^{-1}) with rotating disk electrode (LSV-RDE) of the support and the catalyst at 1600 rpm as well as cyclic voltammograms (50 mV s^{-1}) in oxygen purged 1 M KCl/0.1 M PBS buffer of c) the support und d) the catalyst. The CV as well as LSV-curves are displayed as mean values with standard deviation, represented by the brightly colored areas, of the three different thin-film electrode measurements and all potentials designated as $E_{iR\text{-}corr.}$ were corrected by the uncompensated resistance determined by EIS at 50 kHz. The color key in c) is also valid for b) and d).

used to gain further insight into the chemical composition of the various materials and are shown in Fig. 1a-c and Fig. SI-3. Obviously mostly sp^3-bound oxygen was removed during catalyst formation (Fig. SI-3) and the mainly pyridinic-bound nitrogen of FePc was partially converted to pyrrolic-, quaternary- or graphitic-bound nitrogen (Fig. 1a,b) during the pyrolysis. This leads to the conclusion that the mesomeric ring structure of the phthalocyanine was partly decomposed. Additionally, the binding energy of the Fe 2p peak shifts from 709.2 eV to 710.1 eV (Fig. 1c), which was already reported elsewhere for FePc/CNTs [8]. Hence, the FePc macrocycle was partially destroyed and successfully attached to the MWCNT lattice.

The Raman spectra of support and catalyst are displayed in Fig. 1d and show the characteristic G band (~1590 cm^{-1}), which is related to the sp^2-hybridized structure of the CNT basal planes, as well as a pronounced D band (~1350 cm^{-1}) and a band at ~1620 cm^{-1}, very likely a D'–band, which are both caused by defects in the graphitic lattice due to the non-ideal nanotube structure or edge planes [32–35]. Both samples represent the structure of a defect rich multi-walled CNT material (D:G-ratio = 1.35) which obviously was not affected by the pyrolysis procedure. The D' band superimposes with the G band and therefore cannot be identified unambiguously, but the spectra of catalyst and support are fairly equal to each other, supporting this assignment. The scattering of the two samples slightly differs in the wavenumber region between the D and the G band, which is often denoted as D_3 band (~1500 cm^{-1}), and in the region around the D_4 band (~1200 cm^{-1}), which is overlapping with the very beginning of the D band. The D_3 band is related to amorphous carbon due to functional groups or organic molecules and the D_4 band is attributed to sp^2-sp^3 bonds or C—C and C═C stretching vibrations [32]. In this case, the increase of the D_3:D-ratio (from 0.15 to 0.17) and slight increase of the D_4 band intensity after formation of a Fe-N_x@MWCNT complex by incorporation of the FePc macrocycle into the support can be explained with the Raman scattering of phthalocyanines, which show several sharp peaks in the region of the D_3 and the D_4 band [36]. Due to the high number of recorded spectra and the statistical evaluation for both samples, the small deviations of the spectra are significant [19,37] which is of particular importance for the ongoing discussion in the following.

3.2. Electrochemical characterization and degradation behavior

A two-stage AST protocol was applied to both the support and the catalyst to study their ORR activity and the electrochemical degradation process. The procedure consists of an initial electrochemical characterization step (begin of testing, BoT), followed by 500 AST cycles to 1.57 V vs. RHE (AST1.6) and 2000 AST cycles to 1.87 V vs. RHE (AST1.9) to force highly intense electrochemical stress, as visualized in Fig. 2a. All measurements were performed in phosphate buffer, as explained above. Additionally, the applicability of the prepared catalyst for PEM-FCs is shown by measurements in acidic media (Fig. SI-4a).

The results of AST cycling in oxygen purged 1 M KCl / 0.1 M PBS buffer are summarized in Fig. 2. Cyclic voltammograms of the support (Fig. 2c) at selected levels of the AST protocol (comp. Fig. 2a) show an oxygen reduction peak around 0.35 V vs. RHE unchanged after 500 AST1.6 cycles. After 750 subsequent AST1.9 cycles the ORR peak potential shifts to more positive potentials indicating lower ORR overpotential, and additional peaks between 0.4 and 0.8 V vs. RHE appear which are attributed to oxygen-containing, quinone-type surface groups [38,39]. Additionally, an increased double layer capacity becomes obvious. After 2000 AST1.9 cycles, ORR peak potential shifts to significantly less positive potentials, the surface-group redox peaks disappear, and the double layer capacitance strongly decreases. The CVs of the catalyst clearly differ from those of the support (Fig. 2d). The initial measurement (BoT) shows a more pronounced ORR peak at more positive potentials, indicating much lower ORR overpotential, and an additional oxidation peak (~0.8 V vs. RHE, see also Fig. SI-4b), which originates from oxidation of the Fe^{2+}-species [7]. After 500 AST1.6

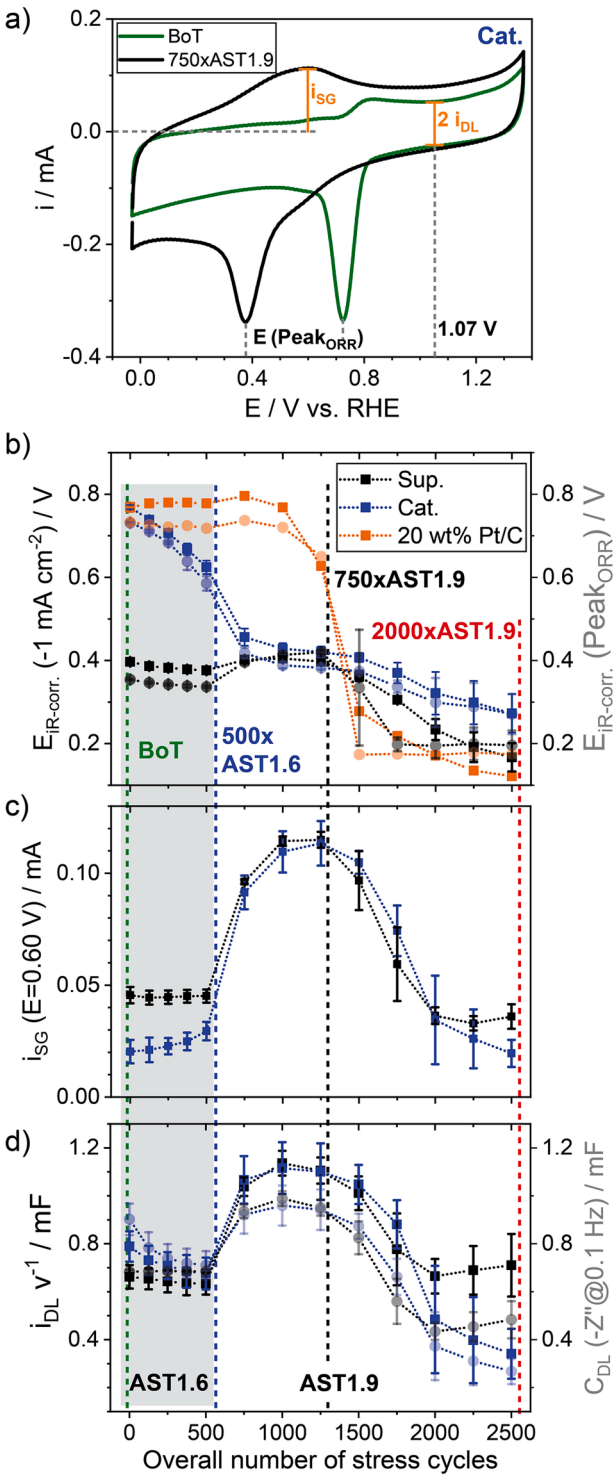

Fig. 3. a) Example of data extraction from CV curves, b) potential at −1 mA cm^{-2}_{geo} extracted from the LSV-RDE curves and the ORR peak potential $E_{iR\text{-}corr.}$(Peak$_{ORR}$) from CVs both shown in Fig. 2 currents due to reactions of surface groups i_{SG} at a given potential and d) the capacitive double layer current i_{DL} at 1.07 V vs. RHE related to the scan rate as well as the electric double layer capacitance derived from EIS with 0.1 Hz at 0.87 V vs. RHE plotted versus the overall number of AST cycles. The color key in b) is also valid for c) as well as d) and the dotted lines in b) to d) are only shown to guide the eye.

cycles this peak has disappeared, and the ORR peak potential is shifted to lower values. Applying 750 AST1.9 cycles causes further decrease of the ORR peak potential, which is however more pronounced than in case of the bare support after the same AST. With ongoing AST1.9 cycling, the CV features of the two samples more and more converge. However, after 2000 AST1.9 cycles the catalyst exhibits stronger collapse of the double layer capacity but still shows a more pronounced ORR peak than the support.

In order to quantify the results of the CV measurements, relevant characteristic data was extracted, as demonstrated in Fig. 3a, including the ohmic drop corrected ORR peak potential ($E_{iR\text{-}corr}(Peak_{ORR})$), the current contribution of the double layer (i_{DL}) and the maximum current contribution of surface groups (i_{SG}). Additionally, the potential at -1 mA cm_{geo}^{-2} was extracted from the LSV-RDE curves at 1600 rpm to compare the ORR performance in the kinetically dominated potential regime (cf. Fig. 2b). All values were taken after every 125 cycles in case of AST1.6 cycling and after every 250 cycles in case of AST1.9 cycling, and the data are summarized in Fig. 3a-d. Fig. 3b visualizes the change of ORR performance during the AST protocol for both samples. For the catalyst, $E_{iR\text{-}corr}(Peak_{ORR})$ as well as $E(-1\ mA\ cm_{geo}^{-2})$ decrease continuously during AST1.6 cycling, but after 500 AST1.6 cycles both are still distinctly higher than that of the support, which remained unchanged. Fig. 3c displays the current in the positive going sweep at ~0.6 V vs. RHE, which increases for the catalyst due to shifting of the ORR onset potential to lower potentials. Simultaneously, the double layer current i_{DL} in CVs and the double layer capacitance C_{DL} determined with EIS at 0.1 Hz decrease and approach that of the support, which remains constant, as can be seen in Fig. 3d (c.f. Fig. SI-5). Cycling to even higher potentials provokes heavy decline of the catalyst's ORR performance, converging with that of the support, which slightly increases likely due to formation of surface groups [27], during the first 250 AST1.9 cycles and i_{SG}, i_{DL} as well as C_{DL} increase for both samples forming a peak with maximum after 750 AST1.9 cycles. During ongoing AST1.9 cycling, the ORR performance of both samples declines, but the catalyst consistently remains slightly more active than the support (Fig. 3b), indicating that the active sites are not completely destroyed during the applied AST, but i_{SG}, i_{DL} as well as C_{DL} however decrease, reaching values even lower than at the BoT. This breakdown is stronger for the catalyst, suggesting that remaining iron impurities catalyze the carbon corrosion of the carbonaceous supporting material as already observed by TG measurements in oxygen containing atmosphere (cf. Fig. SI-1b and corresponding text).

The two-stage AST protocol was also carried out with a commercial platinum-based catalyst (E-TEK®). Its ORR performance, as displayed in Fig. 3b, remains unchanged during AST1.6 cycling, increases slightly during the first 250 AST1.9 cycles and drastically collapses with further AST cycling. It is assumed that the Pt-nanoparticles agglomerate [40] respectively are removed from the carbonaceous support [41] due to the high potentials, causing an ORR performance worse than that of Sup. after 1000 AST1.9 cycles.

3.3. *In situ*-Raman microscopy

To understand the findings from the electrochemical investigations on a molecular basis, structural characterization by Raman spectroscopy was carried out in an *in situ*-setup. *In situ*-Raman mappings were performed at the very same position of the film directly after the initial characterization at the BoT, after 500 AST1.6 cycles as well as after 750 and 2000 AST1.9 cycles. The comparability between the regular and the *in situ*-setup was verified by comparing the shift of the ORR peak in CVs $E_{iR\text{-}corr.}(Peak_{ORR})$ during AST and is shown in Fig. 4a. Moreover, it was verified that the laser irradiation does not impact the electrochemical ($E_{iR\text{-}corr.}(Peak_{ORR})$ and i_{SG}) and structural properties (Raman) of the catalyst by applying electrochemical and Raman characterization without AST cycling (Fig. SI-6 and corresponding text).

As already discussed in chapter 3.1. and shown in Fig. 1d, both samples display the characteristic G band (~1590 cm^{-1}) as well as a pronounced D band (~1350 cm^{-1}) and a D' band (~1620 cm^{-1}) of carbon at the BoT. During AST1.6 cycling, the Raman scattering of the carbonaceous support remains unchanged (cf. Fig. SI-7a), but a slight decrease of the D_3:D-ratio from 0.17 to 0.16 can be observed for the catalyst (Fig. 4b,c), indicating a change in the structure of the carbon-nitrogen compounds of the Fe-N_x@MWCNT moiety as reported before [19,22,23]. 750 AST1.9 cycles result in an increase of the D:G-ratio from 1.35 to 1.57 and a more pronounced D' band for both samples, suggesting the formation of a highly damaged graphitic structure by partial breakup of the MWCNTs conjugated π-electron system [42]. Furthermore, the D_3:D-ratio decreases from 0.15 to 0.12 for the support and from 0.16 to 0.12 for the catalyst, respectively. This might result from the oxidation of the remaining carbon-nitrogen compounds as well as removal of amorphous carbon by electrochemical oxidation [32]. The region of the D_4 band remains unchanged for the support and slightly decreases for the catalyst, so that the two samples show exactly the same Raman spectrum after 750 AST1.9 cycles (Fig. SI-7b). With progressing AST1.9 cycling, no further change can be observed.

3.4. *Ex situ*-X-ray photoelectron spectroscopy (XPS)

X-ray photoelectron spectroscopy was performed *ex situ* at similar levels of the AST protocol as during the *in situ*-Raman studies. For these experiments, the sample ink was drop-casted onto a GC chip ($1 \times 1\ cm^2$) instead of a cylindrical GC disk electrode embedded in PTFE. Due to the changed sample geometry RDE experiments were not possible and the behavior in CV measurements is distinctly different to the measurements in the regular setup, but main changes during AST cycling like disappearance of the ORR and the Fe^{2+}/Fe^{3+} peak, increase of double layer capacitance as well as the formation of surface groups are still clearly visible in this modified setup, as displayed in Fig. SI-8a,b. The advancement of the AST protocol was compared by taking the mass specific oxidation current of the surface groups redox-pair into account (Fig. 5a). Gray squares represent the currents at the regular setup with a Nafion® containing sample film on GC electrode and the dots show the measurement results of the XPS setup. The *ex situ*-XPS setup shows lower reproducibility at the BoT and much higher mass specific currents, which can be explained by lower homogeneity of the suspension, higher surface area of the substrate (1 cm^2 compared to 0.126 cm^2) as well as the lack of electrically non-conducting Nafion®, probably blocking some of the pores of the drop-casted film in the RDE setup. Nevertheless, the development of the surface-group related current during the AST is well comparable, however, the maximum current is achieved after less than AST1.9 cycles (500 compared to 750 in the normal setup) and the decline of the current is faster during subsequent AST1.9 cycling. Therefore, XPS was performed after 500 and 1250 respectively 1500 AST1.9 cycles. For the support, XPS was only performed after AST1.9 cycling, because AST1.6 cycling did not show any impact in previous measurements, and 1500 respectively 2250 AST1.9 cycles were carried out before doing the XPS analysis, because its degradation behavior slightly deviates from that of the catalyst (Fig. SI-8 and text).

As already discussed in chapter 3.1., XPS confirms that iron-nitrogen compounds were attached to the carbonaceous support by wet impregnation of MWCNTs with FePc and that the amount of oxygen decreases due to pyrolysis at 600 °C (Table 2 and Fig. 1). Since electrochemical measurements in 1 M KCl / 0.1 M PBS, containing K^+, Cl^-, HPO_4^{2-} and PO_4^{3-} ions, were performed prior to *ex situ* XPS, K, Cl and P were sometimes present in the XP spectra of the corresponding sample (cf. Fig. SI-9 for survey scans). It is assumed that K and Cl do not have an impact onto the sample's properties and so they were not considered fitting the survey scan. In contrast, P strongly contributes the amount of total oxygen in the sample, due to the oxygen atoms in HPO_4^{2-} and PO_4^{3-} ion, respectively. Therefore, 4 at% oxygen per at% phosphor were subtracted from the measured atomic oxygen concentration to correct the atomic percentage of oxygen in the carbon structure of the sample (Table SI-1 and text).

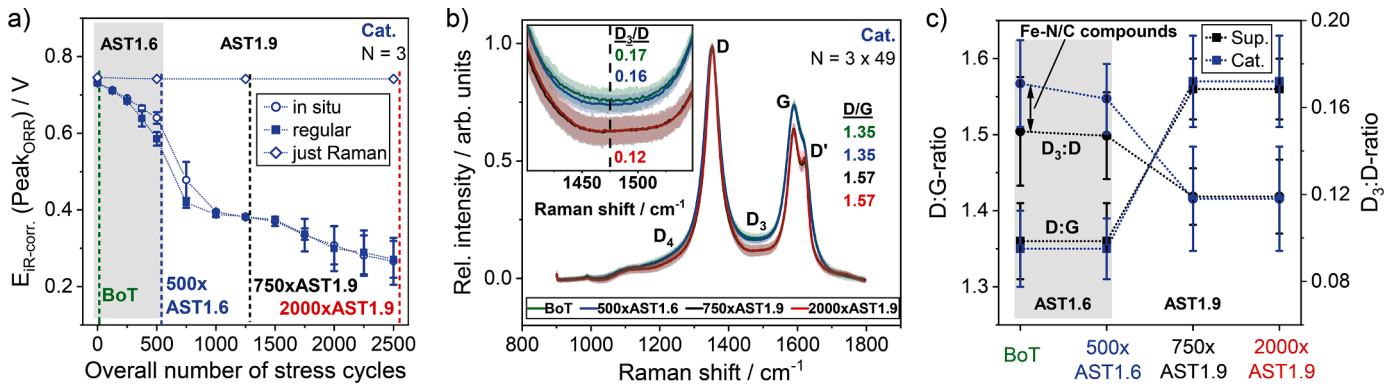

Fig. 4. a) Comparison of the influence of the AST protocol onto ORR activity in the *in situ*-Raman and the regular setup, b) Raman spectra obtained from the catalyst at the BoT, after 500 AST1.6 cycles and 750 respectively 2000 AST1.9 cycles as well as c) D:G- and D_3:D-ratio plotted for the particular AST levels. The magnified graph in b) shows the D_3 band region and the numbers indicate the D_3:D-ratio at 1475 cm^{-1}. The Raman spectra in b) are displayed as average values and standard devation (brightly colored areas) of 49 Raman mapping points each at three separately prepared thin-film electrodes.

The amount of surface-bound oxygen obviously increases (-Fig. 5b-d and Fig. SI-9.) during both AST1.6 and AST1.9 cycling, indicating the formation of surface groups, even during AST1.6 cycling of the catalyst. This contrasts with the electrochemical results, where the development of surface group related currents or an increase of double layer capacitance was not observed for AST1.6 cycling. With proceeding AST1.9 cycling, the oxygen concentration increases only slightly for the catalyst and actually decreases for the support. It is assumed that the maximum amount of oxygen is already reached after 750 AST1.9 cycles which is in good agreement with the development of surface-group related currents as well as double layer capacitance (cf. Fig. 3c,d). The uppermost sample layers, which had the highest amount of oxygen, might also be delaminated due to intercalation processes [43] and subsequently released by washing the sample with water after the electrochemical measurements (cf. chapter 2.2.5.). This could as well explain the decrease in oxygen concentration during subsequent AST1.9 cycling of the support. According to O 1s detail scans, the ratio of sp^3- to sp^2-bound oxygen remains nearly constant for the support, whereas for the catalyst the relative amount of sp^3-bound oxygen strongly decreases and sp^2-bound oxygen (i.e. C═O groups) is formed during AST cycling (Table SI-2 and Fig. SI-10a–g), suggesting a catalytic effect of iron on these processes. Moreover, the amount of P in the survey scan respectively the share of O═P in the O 1s detail scan is clearly higher for the catalyst (Table 3 and Table SI-2). This can be explained by the formation of $FePO_4$ during AST1.6 cycling, since the maximum of the Fe 2p detail scan shifts from 710.2 eV at BoT to approx. 711.8 eV (Fig. 5f), which has been reported as binding energy of $FePO_4$ [44]. Simultaneously, the amount of pyridine-type nitrogen decreases and that of pyrrol-type nitrogen slightly increases (Fig. 5e and Table SI-3), indicating that the Fe-N_x-complex is destroyed by leaching of the iron atom. After applying 750 AST1.9 cycles, the overall amount of nitrogen is strongly reduced (Fig. 5b,e as well as Table 3) and the catalyst exhibits very similar

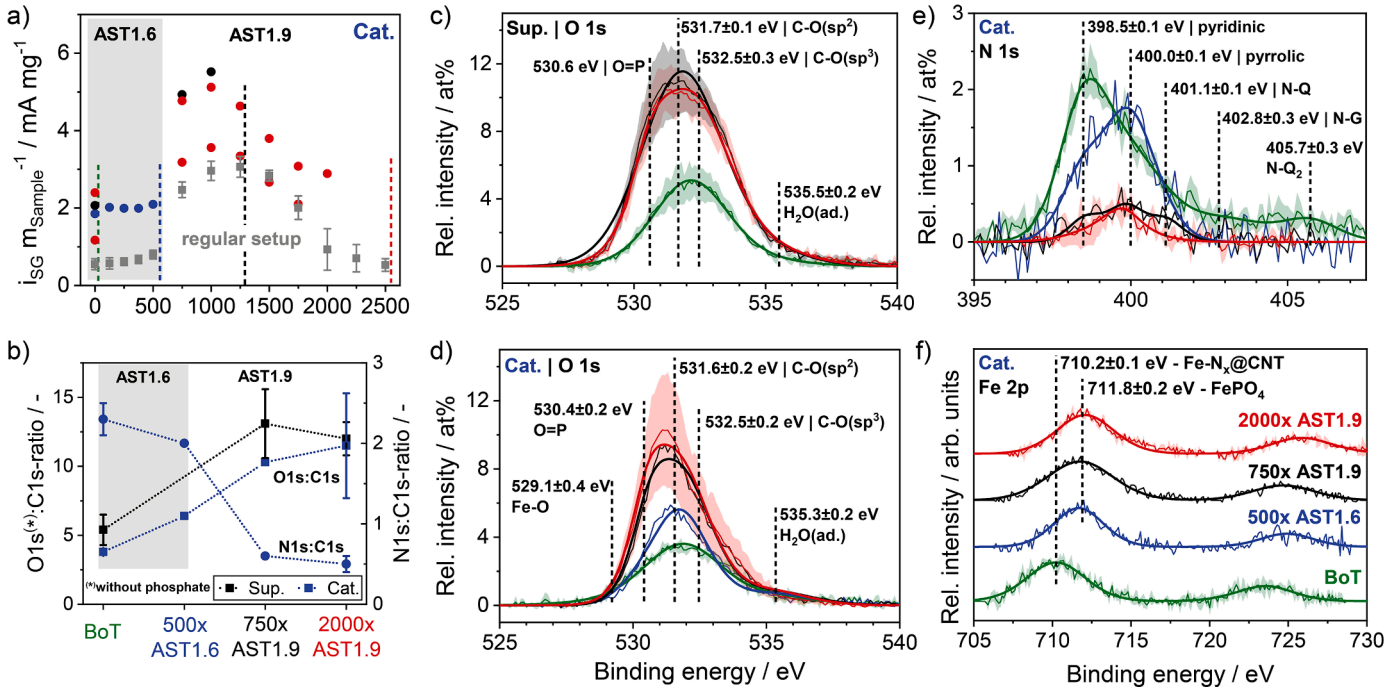

Fig. 5. a) Comparison of the current due to oxygen containing surface-groups during the AST protocol in the regular and the *ex situ* XPS setup, b) change of the O1s:C1s- as well as N1s:C1s-ratio with progressing AST cycling, O 1s detail scans at particular AST levels c) of the support as well as d) the catalyst and e) the N 1s respectively f) the Fe 2p detail scans of the catalyst. The XP spectra are displayed as average values and standard devation (bright colored areas). The number of the respective measurements is given in Table 3.

Table 3
Surface atomic compositions determined by *ex situ*-XPS survey scans at different levels of the AST protocol applied to the supporting material as well as the catalyst for the characteristic binding energies of C 1s (284 eV), O 1s (531 - 532 eV), N 1s (398 - 399 eV), Fe 2p (710 – 713 eV) and P 2p (133 eV).

Sample	C 1s / at%	O 1s[(a)] / at%	N 1s / at%	Fe 2p / at%	P 2p / at%	O 1s[(b)] / at%
Sup.-BoT ($N = 3$)	94.9 ± 1.0	5.1 ± 1.0	–	–	–	5.1 ± 1.0
Sup.−750xAST1.9 ($N = 2$)	88.5 ± 1.8	11.5 ± 1.8	–	–	–	11.5 ± 1.8
Sup.−2000xAST1.9 ($N = 2$)	88.5 ± 2.1	11.3 ± 1.9	–	–	0.2 ± 0.3	10.6 ± 0.8
Cat.-BoT ($N = 3$)	94.1 ± 0.1	3.6 ± 0.1	2.1 ± 0.1	0.1 ± 0.1	–	3.6 ± 0.1
Cat.−500xAST1.6 ($N = 1$)	87.8	9.3	1.8	0.2	0.9	5.6
Cat.−750xAST1.9 ($N = 1$)	83.6	14.1	0.5	0.4	1.4	8.6
Cat.−2000xAST1.9 ($N = 2$)	83.0 ± 0.9	15.0 ± 1.4	0.4 ± 0.0	0.2 ± 0.0	1.4 ± 0.4	9.5 ± 3.1

[(a)] including oxygen in PO_4^{3-}, HPO_4^{2-} and $H_2PO_4^-$.
[(b)] excluding oxygen in PO_4^{3-}, HPO_4^{2-} and $H_2PO_4^-$.

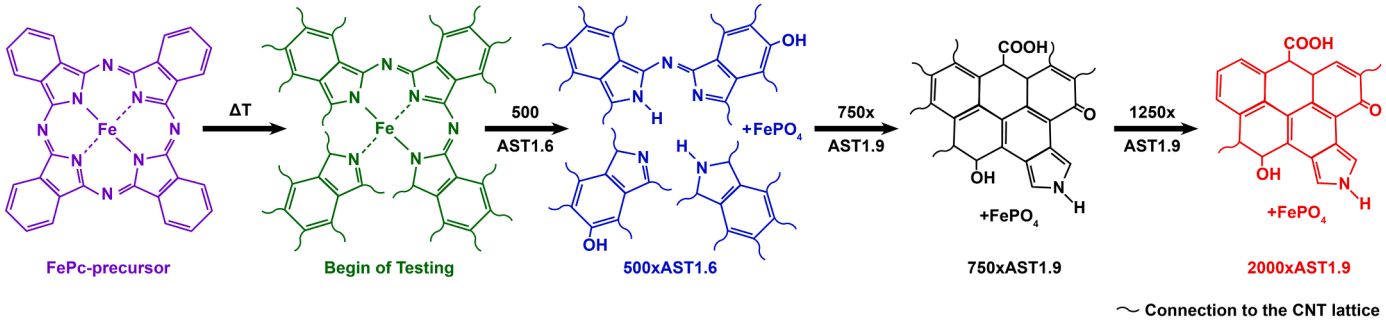

Fig. 6. Proposed degradation mechanism of the investigated Fe-N_x@MWCNT electrocatalyst for the applied two-stage AST protocol in neutral media.

electrochemical and structural properties as the support (cf. chapter 3.2. and 3.3.), suggesting that the C—N-structure is already decomposed. With subsequent AST1.9 cycling the N 1s detail scan changes only slightly, and some nitrogen is still left in the catalyst material after applying the whole AST protocol. This may explain the further on slightly higher activity of the catalyst compared to the support (cf. Fig. 3b).

4. Degradation mechanism and conclusion

An oxygen reduction reaction catalyst was successfully prepared by incorporating iron(II) phthalocyanine into the structure of an oxygen functionalized MWCNT support using wet impregnation followed by pyrolysis at 600 °C. Subsequently, both the catalyst and the bare support were subjected to a two-stage AST protocol, applying potentials between 0.57 and 1.57 V vs. RHE (AST1.6 cycles) and between 0.87 and 1.87 V vs. RHE (AST1.9 cycles). The resulting changes of electrochemical as well as structural properties were investigated with electroanalytical and structural characterization methods.

It is shown that a connection between the FePc macrocycle and MWCNT support is formed during heat treatment without affecting the sp^2-hybridized MWCNT structure and the Fe-N_x-complex critically (Fig. 6, BoT). However already during 500 AST1.6 cycles the attached FePc macrocycle structure is destroyed by leaching out the iron central atom due to formation of $FePO_4$ and the structure of the phthalocyanine ring remains only partly intact. Furthermore, the catalyst is also oxidized at the surface according to XPS, but the defect structure of the MWCNT lattice remains unchanged (Fig. 6, 500xAST1.6) and the performance towards the ORR obviously decreases, albeit it is still higher than for the support. This indicates that the complexed iron atom actually acts as active site for the investigated kind of ORR catalyst in neutral media and not only provides formation of active sites during heat treatment as reported for Fe-N@C catalysts pyrolyzed at higher temperatures [13].

After 750 AST1.9 cycles, the residual structures of the phthalocyanine macrocycle are mostly destroyed, only some nitrogen moieties are left, the surface is heavily oxidized, and defects were inserted into the MWCNT lattice (Fig. 6, 750xAST1.9). Accordingly, the electrochemical double layer capacitance C_{DL} increases, currents due to quinone-type surface-groups emerge and the ORR performance of the catalyst and the support converge, demonstrating that the active sites are removed from the catalyst and the carbonaceous structure of both are affected similarly. With ongoing AST1.9 cycling, the defect structure according to Raman and the atomic surface composition according to XPS stay fairly unchanged for both samples, but electrochemical properties still change. Since C_{DL} decreases and the currents due to surface-groups vanish again, it is assumed that the deeper layers of the sample film, which cannot be investigated by the applied methods, are affected by oxidation and destruction of the sp^2-hybridized structure, leading to a decrease of conductivity and linkage in the sample's backbone (Fig. 6, 2000xAST1.9).

CRediT author statement

S.-J. K. Investigation , Writing - Original Draft
S.-J. K., M.S. and M.B.: Conceptualization, Methodology.
M.S. Supervision
E.D. Investigation
M.B. Supervision
All authors: Writing - Review & Editing

Declaration of competing Interest

The authors declare that they have no known competing financial interests or personal relationships that could have appeared to influence the work reported in this paper.

Data availability

Data will be made available on request.

Acknowledgements

The authors would like to thank Eik Koslowski, Annett Quetschke

and Jenny Bienias-Dragon from our institute for performing XPS, TG and BET measurements.

Supplementary materials

Supplementary material associated with this article can be found, in the online version, at doi:10.1016/j.electacta.2023.142060.

References

[1] Z. Chen, D. Higgins, A. Yu, L. Zhang, J. Zhang, A review on non-precious metal electrocatalysts for PEM fuel cells, Energy Environ. Sci. 4 (2011) 3167, https://doi.org/10.1039/c0ee00558d.

[2] X. Huang, Y. Wang, W. Li, Y. Hou, Noble metal-free catalysts for oxygen reduction reaction, Sci. China Chem. 60 (2017) 1494–1507, https://doi.org/10.1007/s11426-017-9153-6.

[3] M. Bron, S. Fiechter, M. Hilgendorff, P. Bogdanoff, Catalysts for oxygen reduction from heat-treated carbon-supported iron phenantroline complexes, J. Appl. Electrochem. 32 (2002) 211–216, https://doi.org/10.1023/A:1014753613345.

[4] C.W.B. Bezerra, L. Zhang, K. Lee, H. Liu, A.L.B. Marques, E.P. Marques, H. Wang, J. Zhang, A review of Fe–N/C and Co–N/C catalysts for the oxygen reduction reaction, Electrochim. Acta 53 (2008) 4937–4951, https://doi.org/10.1016/j.electacta.2008.02.012.

[5] M. Bron, S. Fiechter, P. Bogdanoff, H. Tributsch, Thermogravimetry/mass spectrometry investigations on the formation of oxygen reduction catalysts for PEM fuel cells on the basis of heat-treated iron phenanthroline complexes, Fuel Cells 2 (2002) 137–142, https://doi.org/10.1002/fuce.200290012.

[6] G. Faubert, G. Lalande, R. Côté, D. Guay, J.P. Dodelet, L.T. Weng, P. Bertrand, G. Dénès, Heat-treated iron and cobalt tetraphenylporphyrins adsorbed on carbon black: physical characterization and catalytic properties of these materials for the reduction of oxygen in polymer electrolyte fuel cells, Electrochim. Acta 41 (1996) 1689–1701, https://doi.org/10.1016/0013-4686(95)00423-8.

[7] H. Xiao, Z.-.G. Shao, G. Zhang, Y. Gao, W. Lu, B. Yi, Fe–N–carbon black for the oxygen reduction reaction in sulfuric acid, Carbon 57 (2013) 443–451, https://doi.org/10.1016/j.carbon.2013.02.017.

[8] R. Cao, R. Thapa, H. Kim, X. Xu, M. Gyu Kim, Q. Li, N. Park, M. Liu, J. Cho, Promotion of oxygen reduction by a bio-inspired tethered iron phthalocyanine carbon nanotube-based catalyst, Nat. Commun. 4 (2013) 2076, https://doi.org/10.1038/ncomms3076.

[9] H. Wang, R. Côté, G. Faubert, D. Guay, J.P. Dodelet, Effect of the pre-treatment of carbon black supports on the activity of Fe-based electrocatalysts for the reduction of oxygen, J. Phys. Chem. B 103 (1999) 2042–2049, https://doi.org/10.1021/jp9821735.

[10] D. Banham, S. Ye, K. Pei, J. Ozaki, T. Kishimoto, Y. Imashiro, A review of the stability and durability of non-precious metal catalysts for the oxygen reduction reaction in proton exchange membrane fuel cells, J. Power Sources 285 (2015) 334–348, https://doi.org/10.1016/j.jpowsour.2015.03.047.

[11] U.I. Kramm, J. Herranz, N. Larouche, T.M. Arruda, M. Lefèvre, F. Jaouen, P. Bogdanoff, S. Fiechter, I. Abs-Wurmbach, S. Mukerjee, J.P. Dodelet, Structure of the catalytic sites in Fe/N/C-catalysts for O2-reduction in PEM fuel cells, Phys. Chem. Chem. Phys. 14 (2012) 11673–11688, https://doi.org/10.1039/c2cp41957b.

[12] M.S. Thorum, J.M. Hankett, A.A. Gewirth, Poisoning the oxygen reduction reaction on carbon-supported Fe and Cu electrocatalysts: evidence for metal-centered activity, J. Phys. Chem. Lett. 2 (2011) 295–298, https://doi.org/10.1021/jz1016284.

[13] K. Strickland, E. Miner, Q. Jia, U. Tylus, N. Ramaswamy, W. Liang, M.-.T. Sougrati, F. Jaouen, S. Mukerjee, Highly active oxygen reduction non-platinum group metal electrocatalyst without direct metal–nitrogen coordination, Nat. Commun. 6 (2015) 7343, https://doi.org/10.1038/ncomms8343.

[14] G. Wan, P. Yu, H. Chen, J. Wen, C.J. Sun, H. Zhou, N. Zhang, Q. Li, W. Zhao, B. Xie, T. Li, J. Shi, Engineering single-atom cobalt catalysts toward improved electrocatalysis, Small 14 (2018) 1–7, https://doi.org/10.1002/smll.201704319.

[15] X. Wan, W. Chen, J. Yang, M. Liu, X. Liu, J. Shui, Synthesis and active site identification of Fe−N−C single-atom catalysts for the oxygen reduction reaction, ChemElectroChem 6 (2019) 304–315, https://doi.org/10.1002/celc.201801302.

[16] A. Zitolo, V. Goellner, V. Armel, M.T. Sougrati, T. Mineva, L. Stievano, E. Fonda, F. Jaouen, Identification of catalytic sites for oxygen reduction in iron- and nitrogen-doped graphene materials, Nat. Mater. 14 (2015) 937–942, https://doi.org/10.1038/nmat4367.

[17] H. Xu, D. Wang, P. Yang, A. Liu, R. Li, Y. Li, L. Xiao, X. Ren, J. Zhang, M. An, Atomically dispersed M-N-C catalysts for the oxygen reduction reaction, J. Mater. Chem. A 8 (2020) 23187–23201, https://doi.org/10.1039/d0ta08732g.

[18] M. Shao, Q. Chang, J.-.P. Dodelet, R. Chenitz, Recent advances in electrocatalysts for oxygen reduction reaction, Chem. Rev. 116 (2016) 3594–3657, https://doi.org/10.1021/acs.chemrev.5b00462.

[19] C. Prössl, M. Kübler, S. Paul, L. Ni, S.-.J. Kinkelin, N. Heppe, K. Eberhardt, C. Geppert, W. Jaegermann, R.W. Stark, M. Bron, U.I. Kramm, Impact of Ir modification on the durability of FeNC catalysts under start-up and shutdown cycle conditions, J. Mater. Chem. A (2021), https://doi.org/10.1039/D1TA04668C.

[20] G. Lalande, G. Faubert, R. Côté, D. Guay, J.P. Dodelet, L.T. Weng, P. Bertrand, Catalytic activity and stability of heat-treated iron phthalocyanines for the electroreduction of oxygen in polymer electrolyte fuel cells, J. Power Sources 61 (1996) 227–237, https://doi.org/10.1016/S0378-7753(96)02356-7.

[21] S. Baranton, C. Coutanceau, C. Roux, F. Hahn, J.-.M. Léger, Oxygen reduction reaction in acid medium at iron phthalocyanine dispersed on high surface area carbon substrate: tolerance to methanol, stability and kinetics, J. Electroanal. Chem. 577 (2005) 223–234, https://doi.org/10.1016/j.jelechem.2004.11.034.

[22] I. Martinaiou, A. Shahraei, F. Grimm, H. Zhang, C. Wittich, S. Klemenz, S. J. Dolique, H.-.J. Kleebe, R.W. Stark, U.I. Kramm, Effect of metal species on the stability of Me-N-C catalysts during accelerated stress tests mimicking the start-up and shut-down conditions, Electrochim. Acta 243 (2017) 183–196, https://doi.org/10.1016/j.electacta.2017.04.134.

[23] U.I. Kramm, A. Zana, T. Vosch, S. Fiechter, M. Arenz, D. Schmeißer, On the structural composition and stability of Fe–N–C catalysts prepared by an intermediate acid leaching, J. Solid State Electrochem. 20 (2016) 969–981, https://doi.org/10.1007/s10008-015-3060-z.

[24] M.A.C. de Oliveira, V.C.A. Ficca, R. Gokhale, C. Santoro, B. Mecheri, A. D'Epifanio, S. Licoccia, P. Atanassov, Iron(II) phthalocyanine (FePc) over carbon support for oxygen reduction reaction electrocatalysts operating in alkaline electrolyte, J. Solid State Electrochem. 25 (2021) 93–104, https://doi.org/10.1007/s10008-020-04537-x.

[25] A. Morozan, S. Campidelli, A. Filoramo, B. Jousselme, S. Palacin, Catalytic activity of cobalt and iron phthalocyanines or porphyrins supported on different carbon nanotubes towards oxygen reduction reaction, Carbon 49 (2011) 4839–4847, https://doi.org/10.1016/j.carbon.2011.07.004.

[26] C. Santoro, R. Gokhale, B. Mecheri, A. D'Epifanio, S. Licoccia, A. Serov, K. Artyushkova, P. Atanassov, Design of iron(II) phthalocyanine-derived oxygen reduction electrocatalysts for high-power-density microbial fuel cells, ChemSusChem 10 (2017) 3243–3251, https://doi.org/10.1002/cssc.201700851.

[27] M. Steimecke, S. Rümmler, M. Bron, The effect of rapid functionalization on the structural and electrochemical properties of high-purity carbon nanotubes, Electrochim. Acta 163 (2015) 1–8, https://doi.org/10.1016/j.electacta.2015.02.142.

[28] H. Schulenburg, S. Stankov, V. Schünemann, J. Radnik, I. Dorbandt, S. Fiechter, P. Bogdanoff, H. Tributsch, Catalysts for the oxygen reduction from heat-treated iron(III) tetramethoxyphenylporphyrin chloride: structure and stability of active sites, J. Phys. Chem. B 107 (2003) 9034–9041, https://doi.org/10.1021/jp030349j.

[29] V. Datsyuk, M. Kalyva, K. Papagelis, J. Parthenios, D. Tasis, A. Siokou, I. Kallitsis, C. Galiotis, Chemical oxidation of multiwalled carbon nanotubes, Carbon 46 (2008) 833–840, https://doi.org/10.1016/j.carbon.2008.02.012.

[30] J.L. Hueso, J.P. Espinós, A. Caballero, J. Cotrino, A.R. González-Elipe, XPS investigation of the reaction of carbon with NO, O2, N2 and H2O plasmas, Carbon 45 (2007) 89–96, https://doi.org/10.1016/j.carbon.2006.07.021.

[31] K. Artyushkova, A. Serov, S. Rojas-Carbonell, P. Atanassov, Chemistry of multitudinous active sites for oxygen reduction reaction in transition metal–nitrogen–carbon electrocatalysts, J. Phys. Chem. C 119 (2015) 25917–25928, https://doi.org/10.1021/acs.jpcc.5b07653.

[32] A. Sadezky, H. Muckenhuber, H. Grothe, R. Niessner, U. Pöschl, Raman microspectroscopy of soot and related carbonaceous materials: spectral analysis and structural information, Carbon 43 (2005) 1731–1742, https://doi.org/10.1016/j.carbon.2005.02.018.

[33] Y. Wang, D.C. Alsmeyer, R.L. McCreery, Raman spectroscopy of carbon materials: structural basis of observed spectra, Chem. Mater. 2 (1990) 557–563, https://doi.org/10.1021/cm00011a018.

[34] M.S. Dresselhaus, A. Jorio, M. Hofmann, G. Dresselhaus, R. Saito, Perspectives on carbon nanotubes and graphene Raman spectroscopy, Nano Lett. 10 (2010) 751–758, https://doi.org/10.1021/nl904286r.

[35] M.M. Lucchese, F. Stavale, E.H.M. Ferreira, C. Vilani, M.V.O. Moutinho, R. B. Capaz, C.A. Achete, A. Jorio, Quantifying ion-induced defects and Raman relaxation length in graphene, Carbon 48 (2010) 1592–1597, https://doi.org/10.1016/j.carbon.2009.12.057.

[36] R. Aroca, D.P. Dilella, R.O. Loutfy, Raman spectra of solid films—I, J. Phys. Chem. Solids 43 (1982) 707–711, https://doi.org/10.1016/0022-3697(82)90235-9.

[37] S. Rümmler, M. Steimecke, S. Schimpf, M. Hartmann, S. Förster, M. Bron, Highly Graphitic, Mesoporous carbon materials as electrocatalysts for vanadium redox reactions in all-vanadium redox-flow batteries, J. Electrochem. Soc. 165 (2018) A2510–A2518, https://doi.org/10.1149/2.1251810jes.

[38] K. Tammeveski, K. Kontturi, R.J. Nichols, R.J. Potter, D.J. Schiffrin, Surface redox catalysis for O2 reduction on quinone-modified glassy carbon electrodes, J. Electroanal. Chem. 515 (2001) 101–112, https://doi.org/10.1016/S0022-0728(01)00633-7.

[39] N. Alexeyeva, K. Tammeveski, Electrochemical reduction of oxygen on multiwalled carbon nanotube modified glassy carbon electrodes in acid media, Electrochem. Solid State Lett. 10 (2007) F18, https://doi.org/10.1149/1.2713657.

[40] M.F. Labata, G. Li, J. Ocon, P.-Y.A. Chuang, Insights on platinum-carbon catalyst degradation mechanism for oxygen reduction reaction in acidic and alkaline media, J. Power Sources 487 (2021), 229356, https://doi.org/10.1016/j.jpowsour.2020.229356.

[41] F.J. Perez-Alonso, C.F. Elkjær, S.S. Shim, B.L. Abrams, I.E.L. Stephens, I. B. Chorkendorff, Identical locations transmission electron microscopy study of Pt/C electrocatalyst degradation during oxygen reduction reaction, J. Power Sources 196 (2011) 6085–6091, https://doi.org/10.1016/j.jpowsour.2011.03.064.

[42] I.D. Rosca, F. Watari, M. Uo, T. Akasaka, Oxidation of multiwalled carbon nanotubes by nitric acid, Carbon 43 (2005) 3124–3131, https://doi.org/10.1016/j.carbon.2005.06.019.
[43] P. Yu, S.E. Lowe, G.P. Simon, Y.L. Zhong, Electrochemical exfoliation of graphite and production of functional graphene, Curr. Opin. Colloid Interface Sci. 20 (2015) 329–338, https://doi.org/10.1016/j.cocis.2015.10.007.
[44] R.L. McCormick, G.O. Alptekin, Comparison of alumina-, silica-, titania-, and zirconia-supported FePO4 catalysts for selective methane oxidation, Catal. Today 55 (2000) 269–280, https://doi.org/10.1016/S0920-5861(99)00243-6.